Submitted for the Proceedings of the SPIE Conference on Remote Sensing, held in Amsterdam, 3-6 September 2023

Second derivative water reflectance spectra for phytoplankton species detection – origin, impact and removal of spectral wiggles

Kevin G. Ruddick*[a], Pieter De Vis[b], Clémence Goyens[a], Joel Kuusk[c], Héloise Lavigne[a] and Quinten Vanhellemont[a]

[a]Royal Belgian Institute of Natural Sciences (RBINS), 29 Rue Vautierstraat, 1000 Brussels, Belgium;

[b]National Physical Laboratory (NPL), Teddington, United Kingdom;

[c]Tartu Observatory, University of Tartu, Tõravere, 61602 Tartu county, Estonia

*kruddick@naturalsciences.be

ABSTRACT

The new generation of spaceborne hyperspectral sensors offers the potential to provide new information on water quality, especially regarding phytoplankton groups. While phytoplankton species composition algorithms are easily demonstrated in model studies, the application of algorithms to spaceborne data may be much more challenging because of processing artefacts in the spectral vicinity of atmospheric absorption features. If not treated carefully, the unresolved spectral variability of radiance and irradiance can create spectral artefacts ("wiggles") in water reflectance spectra with high second derivative and thus contaminates pigment detection algorithms. In this study one of the processes generating such spectral wiggles is explained for an in situ radiometer system with a wavelength offset between the radiance and irradiance measurements. The two measurements used to calculate reflectance are differently affected by narrow, unresolved atmospheric absorption bands. Removal or reduction of such wiggles could be achieved by physically-based weighting in the spectral interpolation of irradiance rather than the typical spectral averaging generally used to hide such problems when using linear interpolation. Although demonstrated here for in situ radiometry the need for careful treatment of unresolved spectral variability in spaceborne data is raised, particularly if such data is used for second derivative algorithms which are very sensitive to short wavelength scale variability.

Keywords: hyperspectral, spectral wiggles, phytoplankton pigments, second derivative, reflectance, absorption, noise

1. INTRODUCTION

1.1 Motivation – using hyperspectral spaceborne data for phytoplankton species detection

The new generation of spaceborne hyperspectral sensors DESIS[1], PRISMA[2], ENMAP[3], PACE[4], offers the potential to provide new information on coastal and inland water quality. A major potential advantage of hyperspectral, compared with multispectral, data is the enhanced possibility to detect individual phytoplankton pigments and thus better discriminate between different phytoplankton groups. Phytoplankton pigments are typically seen in water reflectance spectra by a reduction in reflectance over a limited spectral range, e.g. 15-50 nm, corresponding to the pigment absorption spectrum. While phytoplankton species composition algorithms are easily demonstrated in model studies with simulated data, the application of algorithms to spaceborne data may be much more challenging. Algorithms for phytoplankton pigment detection typically rely, explicitly or implicitly, on the second derivative of water reflectance in wavelength space. In the case of spaceborne data, solar Fraunhofer lines and absorption from terrestrial atmospheric gases typically have much narrower spectral width than the Full Width Half Max (FWHM) of the Spectral Response Function (SRF) of spaceborne sensors used/proposed for aquatic remote sensing, e.g. HYPERION, CHRIS, DESIS, ENMAP, PACE, CHIME, GLIMR, etc. If not treated carefully, this creates spurious spectral variability ("wiggles") in water reflectance spectra with high second derivative and thus contaminates pigment detection algorithms.

1.2 Scope

The scope of this paper is the study of natural processes and data processing artefacts affecting the second derivative of hyperspectral water reflectance for the wavelength range 400-900 nm as measured by in situ or spaceborne spectrometers

with spectral resolution between 1 nm and 10 nm FHWM. The cause of artefacts, termed here "spectral wiggles", near unresolved atmospheric absorption bands is studied in detail.

While the motivation is provided by the application of phytoplankton species detection from in situ and spaceborne hyperspectral data the approach is essentially generic and is relevant also to hyperspectral land surface reflectance, e.g. when using derivative spectroscopy for plant pigment analysis[5], and to the use of in situ reflectance for satellite cal/val.

The wavelength range 380-400 nm may also be useful for this or other aquatic applications and the wavelength range 900-2400 nm may be useful for other terrestrial applications. While the approach of this paper can easily be extended to other wavelength ranges the current focus is on 400-900 nm because of the availability of high quality in situ water reflectance spectra in that range [6–8].

For spectrometers with spectral resolution finer than 1 nm the present study is less relevant because spectral features caused by absorbing atmospheric gases and/or solar Fraunhofer lines may be spectrally resolved (although wiggles can still be generated in higher resolution reflectance spectra if radiance and irradiance have different SRF).

1.3 Spectral "wiggles" in hyperspectral data

Hyperspectral water reflectance spectra measured by satellites (with atmospheric correction) or by abovewater radiometry (with skyglint correction) are often not smooth, showing short wavelength scale variations, e.g. Figure 1, which shows both smooth spectral variability associated with natural in-water absorption processes as well as a spurious wiggle near 762 nm. In addition to that wiggle apparent even in the original reflectance spectrum, more wiggles become apparent when the same data is presented as the difference between the original reflectance and a spectrally-smoothed reflectance – see top-right panel of Figure 1. As will be seen later, these difference ("original-averaged") spectra contain both artefacts and residues of natural processes, indicating that artefact-removal by spectral smoothing with a moving average also removes some of the desired signal.

These short wavelength scale variations are often referred to as "noise", although such terminology is misleading if the variation is not random but is spectrally structured. In the present paper the term "wiggle" will be used for all short wavelength scale variations.

We use here the definition of water-leaving radiance reflectance, ρ_w, as:

$$\rho_w = \frac{\pi L_w}{E_d} \tag{1}$$

Where L_w is the water-leaving radiance (with air-water interface reflection removed) and E_d is the planar downwelling irradiance just above the water surface.

For the example dataset presented in Figure 1 and fully documented in [6], the second derivative of reflectance is calculated using a centered finite difference method:

$$\left.\frac{\partial^2 \rho_w}{\partial \lambda^2}\right|_{\lambda^i} = \frac{(\rho_w^{i+K} - 2 * \rho_w^i + \rho_w^{i-K})}{h^2} \tag{2}$$

on a regular wavelength grid with step size,

$$h = \lambda^{i+K} - \lambda^i = \lambda^i - \lambda^{i-K} \tag{3}$$

Application of a standard 2nd derivative using adjacent wavelengths (i.e. $K = 1, h = 1\ nm$ for this dataset) can generate very noisy results, which are typically smoothed either by averaging before taking the derivative or taking the derivative over a wider wavelength basis, e.g. $K = 5, h = 5\ nm$, or both, as illustrated in Figure 2 and Figure 3.

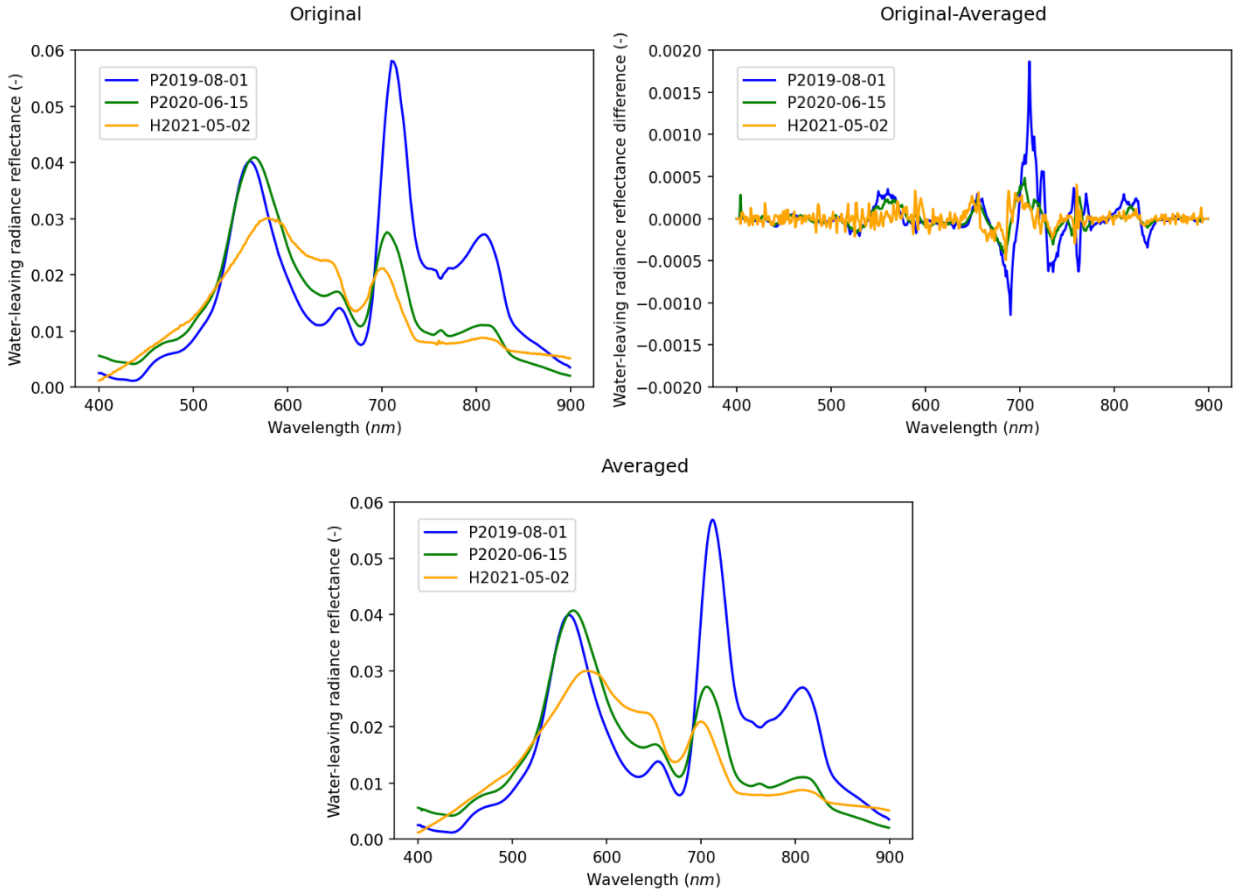

Figure 1. Water-leaving radiance reflectance spectra, ρ_w, from the HYPSTAR® ("H" in legend) and PANTHYR ("P" in legend) radiometer systems at Blankaart water reservoir on 3 different dates. [top-left] Data processed to a regular 1 nm grid from 400-900 nm as described for Figure 11 of 6. [bottom] Original data post-processed with a moving average filter of width 10 nm [top-right] Difference between original and averaged data

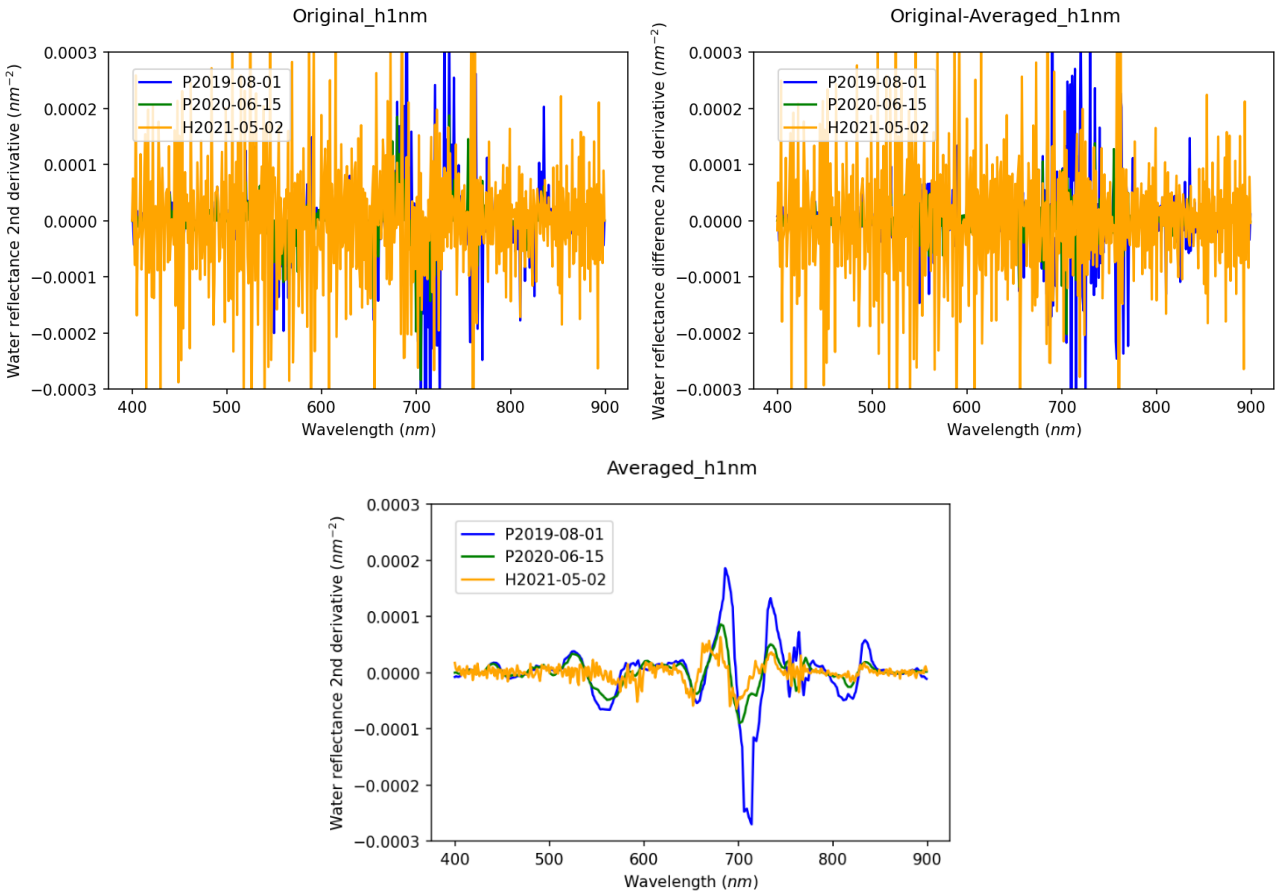

Figure 2. Second derivative of water reflectance spectra from Figure 1 using a narrow step, $h = 1\ nm$, calculated from [top-left] original spectra, [bottom] 10 nm-averaged spectra [top-right] difference between original and averaged spectra.

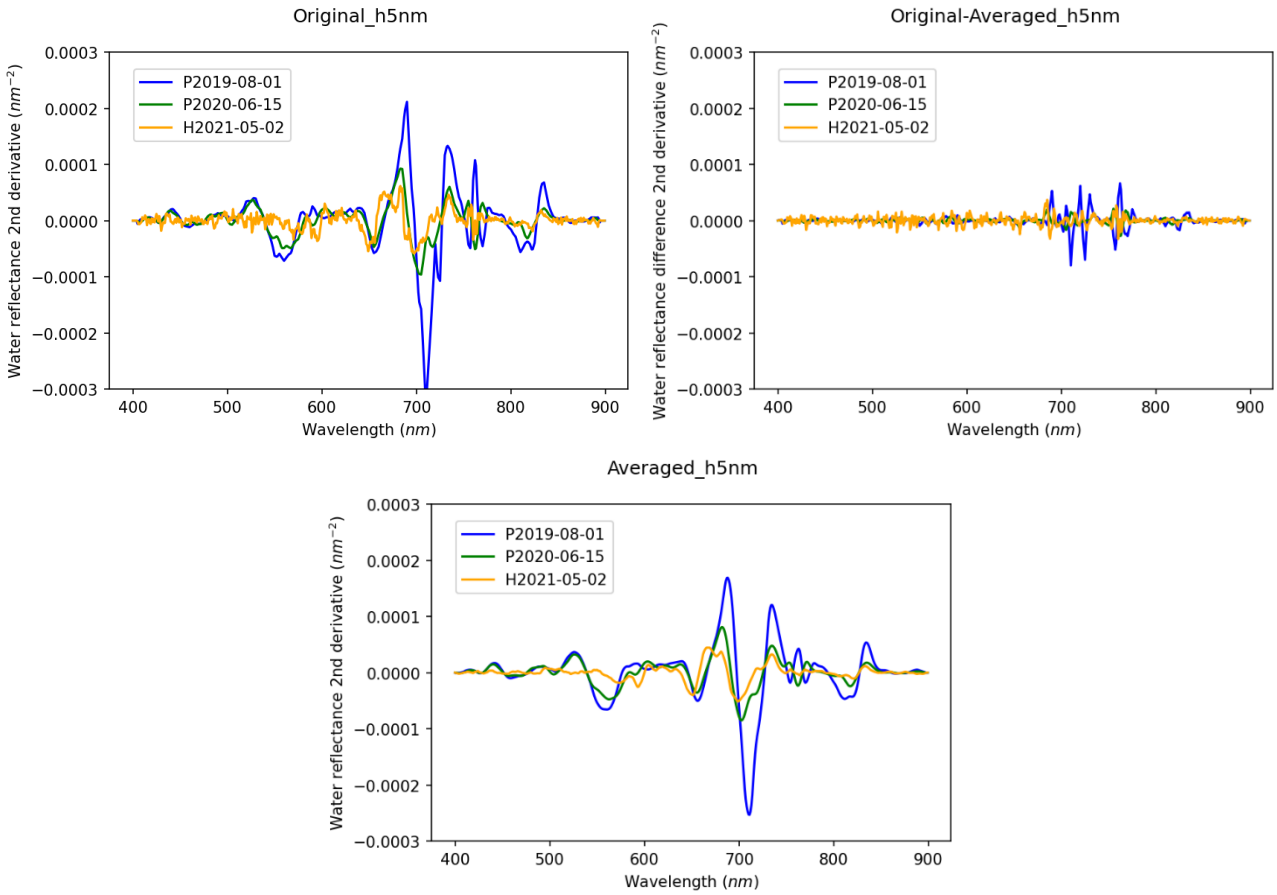

Figure 3. As Figure 2 but with second derivative calculated using a wider step, $h = 5\ nm$.

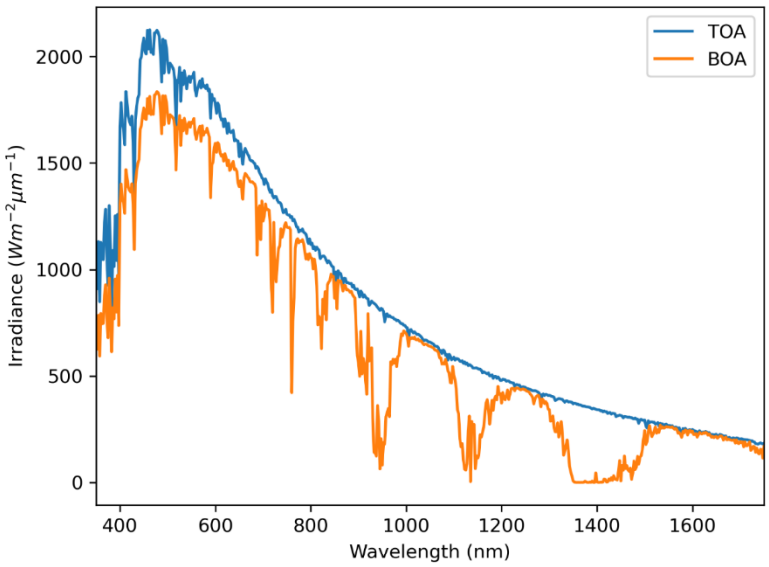

Figure 4. Sample planar downwelling irradiance spectrum at top of atmosphere (TOA: blue) and bottom of atmosphere (BOA:orange) simulated by 6SV[9] version 2.1 with following conditions: *2.5 nm* spacing, TSIS HSRS version 2 TOA spectrum[10] at *1 nm* linearly interpolated to 6SV spacing, aerosol model 1 "Continental", aerosol optical thickness at 550 nm =0.15, sun zenith angle=30°, standard atmospheric pressure (1013.25 hPa), water vapour 1.5 g/cm2, ozone 300 DU, other gases fixed using 6SV defaults.

For many applications, e.g. use of single band turbidity retrieval[11] or two/three band red/near infrared chlorophyll a retrieval algorithms [12,13], wiggles in the input water reflectance spectrum may be a minor embarrassment when presenting spectra but may not have a significant impact on results. In contrast, the use of second derivative algorithms or line height algorithms for phytoplankton species detection may be very sensitive to wiggles [14] since the second derivative is proportional to the amplitude of a reflectance gradient variation but inversely proportional to the spectral width of a feature. The shorter the wavelength scale of a process/feature, the greater is the second derivative.

The impact of wiggles on the second derivative of water reflectance can be reduced by prior spectral averaging of the water reflectance data and/or by choosing a wider wavelength range, e.g. 10 nm, for numerical discretization of the second derivative. In both approaches the choice of averaging/discretization range needs to be made carefully to remove the unwanted wiggle without attenuating the wanted signal. Other approaches consist in developing empirical methods to correct this effect [15–17] without trying to fully understand it. In the current paper, spectral averaging is eschewed in favour of understanding the processes generating wiggles and dealing with them in a more appropriate manner.

1.4 Spectral width of aquatic processes

In this section we consider the spectral width of aquatic processes with the aim of summarizing processes which are spectrally well-resolved by a sensor with 10 nm FWHM and spectral sampling every 3 nm, and those which are not well-resolved. The well-resolved processes are termed "(spectrally) smooth" in this paper.

Theoretical models of water reflectance are generally based on the absorption and elastic backscattering of light by phytoplankton, non-algae particles (NAP), Coloured Dissolved Organic Matter (CDOM) and pure water (H_2O) molecules.

Inelastic processes, including Raman scattering, fluorescence, phosphorescence, and bioluminescence also occur in water but are generally weak, compared to the elastic scattering, and spectrally fairly smooth. Such processes will be neglected in the present study.

Consider one by one the absorption and elastic scattering processes:

- The absorption spectra for NAP and CDOM are generally modelled by an exponentially decreasing function of wavelength over the range 400-900 nm [18–21] and the absorption spectrum for H_2O is generally taken from laboratory measurements[22]. These spectra are spectrally smooth.
- The absorption spectrum for phytoplankton is composed of absorption from various pigments, which may vary in relative concentration between phytoplankton species, thus raising the potential for retrieving information on phytoplankton species composition from measurements of absorption or, more challengingly, water reflectance. The spectral width of phytoplankton pigment absorption is generally 15-50 nm FWHM and is thus considered smooth in the present paper.
- The backscattering spectrum for NAP and for H_2O are generally modelled by a power law function of wavelength and are spectrally smooth.
- The backscattering spectrum for phytoplankton is often modelled as spectrally flat or very smooth [23]. In more complex models taking account of anomalous diffraction processes[24] the phytoplankton backscatter spectrum is affected by absorption processes and shows spectral features with width of the corresponding features in the phytoplankton absorption spectrum.

As shown in the example of Figure 5, all of the abovementioned processes can be considered spectrally smooth, i.e., well-resolved by a sensor with 10 nm FWHM. It is therefore not surprising that the vast majority of hyperspectral "ocean colour" satellites and hyperspectral in situ measurements of water reflectance are based on spectrometers with typical spectral response of 10 nm FWHM, or 5 nm FWHM in the case of PACE.

Interestingly the pure water absorption, which dominates the total absorption coefficient in the longer wavelengths ($\lambda > 600\ nm$), has a significant second derivative, but is expected to be rather constant in space and time, notwithstanding slight changes with salinity and temperature[25]. The simulations of Figure 5 also demonstrate that care will be needed in defining simulation inputs when analysing second derivatives. Tabulated datasets and/or sudden gradient changes in inputs may not be obvious when considering water reflectance, but become more visible in the second derivative – see the impact of non-exponential mineral absorption coefficients, a_{MIN} on second derivative of absorption and hence reflectance in the range 430-480 nm and 560-600 nm in Figure 5.

The second derivative of a water reflectance spectrum will amplify (with respect to the reflectance spectrum itself) any features generated by processes with narrow spectral width. Thus, from the abovementioned absorption and elastic backscattering processes, the second derivative water reflectance spectrum will show more clearly the impact of absorption by phytoplankton pigments [26,27].

On the basis of in situ absorption measurements, the fourth derivative has been suggested[26,28] as relevant for phytoplankton pigment quantification with better separation between overlapping pigments than the second derivative. However, the fourth derivative is likely to be even more problematic than the second derivative when applied to spaceborne water reflectance measurements.

The second derivative of water reflectance has therefore been proposed for use in remote sensing algorithms of phytoplankton species composition, e.g. [29–32,14], and is the focus in the present paper. Other algorithms for phytoplankton species composition may use other data manipulations than the second derivative approach considered here but will also generally also be affected by processes with variability at short wavelength scales.

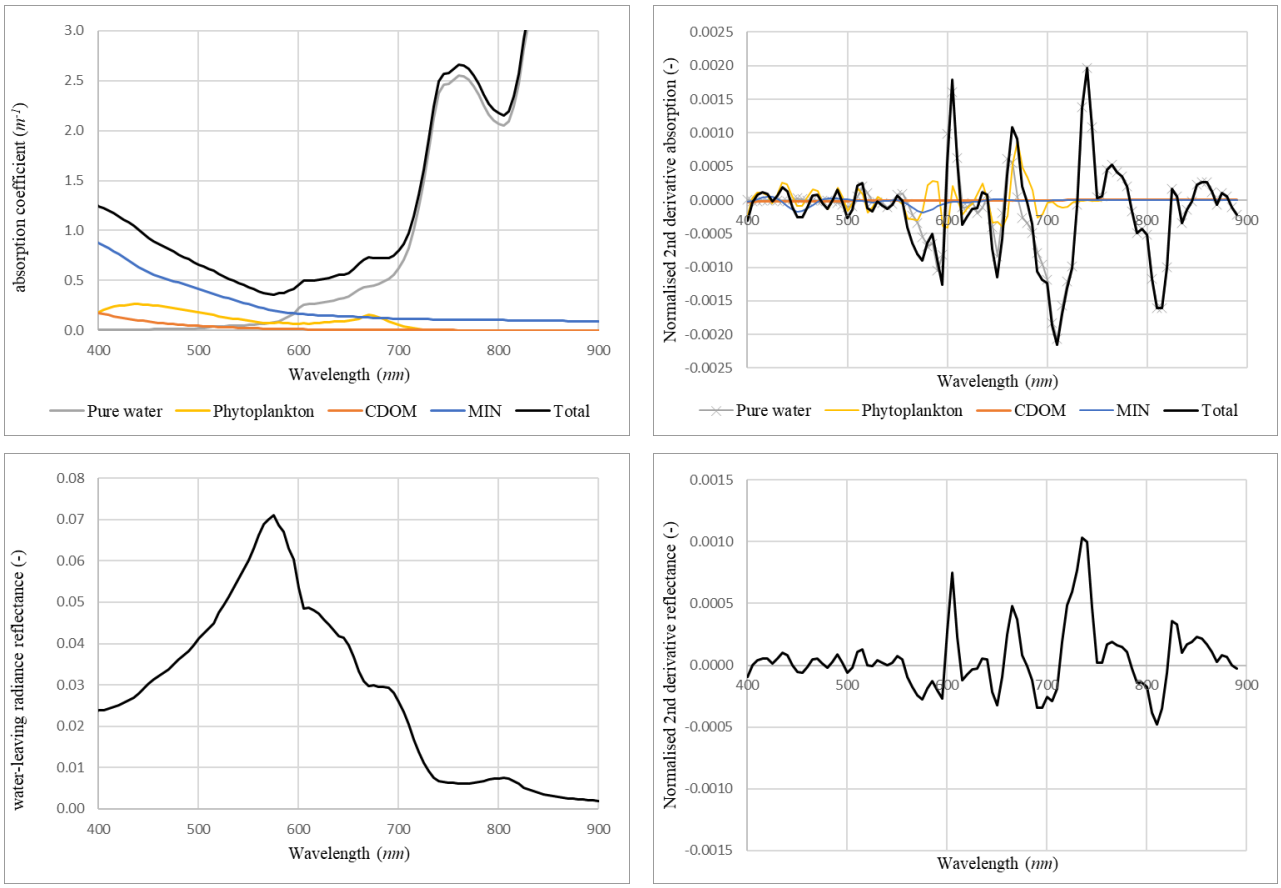

Figure 5. Example of spectra for a simulation made with the HYDROLIGHT 5.3 radiative transfer software[33]. (top-left) Total absorption coefficient, a_t, decomposed into pure water, a_w, phytoplankton, a_ϕ, CDOM, a_{CDOM} and mineral absorption coefficients, a_{MIN}; (top-right) negative normalized second derivative absorption spectra $-a_t \partial^2 a_X / \partial \lambda^2$ where $X = t, w, \phi, CDOM, MIN$ for the total and the four components of absorption respectively; (bottom-left) water-leaving radiance reflectance, ρ_w, and (bottom-right) normalized second derivative reflectance $(1/\rho_w) * \partial^2 \rho_w / \partial \lambda^2$. Simulations are for concentrations Chlorophyll a $= 10$ µ$g\ l^{-1}$, $a_{CDOM}(440\ nm) = 0.1\ m^{-1}$, mineral particles MIN$= 10\ mg\ l^{-1}$, no inelastic scattering and Inherent Optical Property models: pure water absorption[34,35], Case 1 phytoplankton absorption, exponentially decreasing a_{CDOM} with exponent $0.014\ nm^{-1}$ and various other defaults. Simulations made from $380\ nm$ to $900\ nm$ with $5\ nm$ sampling. Second derivative calculated by centered finite difference with step $h = 10\ nm$.

1.5 Spectral width of other processes.

While the water reflectance spectrum from a theoretical model, as outlined in section 1.4, will generally be spectrally smooth, with the second derivative showing mainly the phytoplankton pigments and pure water absorption, measured water reflectance spectra often have considerable variability at short wavelength scales. This variability may appear at one or more atmospheric absorption bands, e.g. the "blip" often found in 3-sensor TRIOS/RAMSES (10 nm FWHM) measurements near 762 nm – see Figure 7 of [36], may appear as "wiggles" throughout the spectrum … or may be hidden by spectral averaging in the data processing.

While smoothing of water reflectance data, by spectral averaging or similar low-pass filtering, is often adopted by scientists needing quick results but confronted with measurements that do not "look nice", spectral averaging may also attenuate or remove relevant information. The approach of the present study is rather "Don't suppress the wiggles they're telling you something!" [37]. A better understanding of the processes generating spectral variability at short wavelength scales can lead to physically based data processing and ensure that the desired signal, here relating to phytoplankton pigment absorption, is not modified by any smoothing processes.

Short wavelengths scale variability is, of course, present naturally in BOA and TOA downwelling irradiance spectra (Figure 4) but does not necessarily appear in water reflectance measurements. For example, if a single radiance sensor is used to measure both upwelling radiance and downwelling irradiance, the latter by measuring upwelling radiance from a horizontal plaque of known reflectance[38–40], then the wiggles in radiance and irradiance may cancel to give a smooth water reflectance.

The non-aquatic processes that can generate spectral variability of water reflectance at short wavelength scales, termed hereafter "wiggles", are discussed in this section.

Random noise, often temperature-related, is encountered in opto-electronic devices such as spectrometers and should be reduced to levels which do not contaminate end-user products. Reduction of random noise is generally achieved already via the technical specification used in sensor design or may be achieved a posteriori by spatio-temporal averaging for spaceborne sensors [41] or by averaging over replicates for in situ radiometers. Spectral averaging will also reduce random noise but is generally not appropriate because it also reduces spectral resolution.

Interband calibration for multispectral spaceborne and in situ radiometers is usually assumed to be achieved by the absolute responsivity calibration, although it may be analysed separately[42–44]. For hyperspectral measurements where derivative-based algorithms may be used it becomes relevant to have an interband calibration requirement[15–17] in addition to the typical absolute responsivity calibration requirements, e.g. an interband calibration accuracy requirement of 0.25% or better at top of atmosphere has been suggested[14] for application of the Modified Astoreca Index for detection of *Phaeocystis globosa*. Nonlinearity of the sensor which typically depends on the raw signal level can also affect the interband calibration accuracy[45,46], especially for very strong and sharp features like the 762 nm oxygen absorption band.

Spectral Response Function (SRF) differences between the radiance and irradiance measurements used to derive water reflectance from in situ radiometry can generate wiggles as will be seen in this paper.

Abovewater downwelling irradiance in satellite data processing is generally derived from tabulated data for the extraterrestrial solar irradiance [47] and downward atmospheric transmittance derived from a radiative transfer model using information on aerosols and absorbing gas concentrations derived from the satellite radiance measurement and/or extraneous sources (meterological data, sunphotometer data, etc.). The modelled irradiance is then spectrally convolved over the SRF of the satellite radiometer. Any errors in the assumed SRF used for irradiance and the actual SRF of the radiance measurement may generate wiggles, especially for wavelengths with high spectral variability of downwelling irradiance, E_d, i.e. near wavelengths with high atmospheric absorption and/or near solar Fraunhofer lines. Such errors may be significant since the SRF of a spaceborne spectrometer is generally a complex function of cross-track pixel, e.g. "smile" [48]. Errors in the tabulated extraterrestrial solar irradiance may also generate wiggles.

Concentrations of absorbing gases are used as input for the atmospheric correction of spaceborne data both for water-leaving radiance and for the modelling of downwelling irradiance. Errors in these concentration inputs may also generate wiggles in the water reflectance.

1.6 Summary of processes generating wiggles in water reflectance spectra

A summary of the processes described in the previous sections is given in Table 1.

Table 1 Summary of wiggle-generating processes for water reflectance spectra.

Process	**In situ/ Satellite**	**Signature**	**Solution**
Phytoplankton Pigment absorption	Both	15-50 nm width around known absorption wavelengths	Desired signal
Random noise	Both	Random in space, time, wavelength	Spectrometer design (signal:noise) In Situ: replicate averaging Sat: spatial/temporal averaging Both: spectral averaging
Interband calibration	Both	Systematic wavelength variation	Improve interband calibration (design specification, pre-launch cal, vicarious cal)
Measured radiance/irradiance SRF difference	In situ	Wiggles near unresolved spectral features (absorbing gases)	Spectral interpolation weighted with typical irradiance – this paper
Measured radiance/modelled irradiance SRF difference	Satellite	As above	Consideration of unresolved spectral variability at all relevant processing steps
Errors in absorbing gas concentrations	Satellite	As above	As above

1.7 Overview of paper

In this paper we demonstrate with model simulations how a Spectral Response Function (SRF) differences between the radiance and irradiance measurements can generate undesirable wiggles with significant impact on the second derivative of water reflectance.

2. METHOD

2.1 Definition of surface reflectance

Here we simulate a pointable radiometer used to measure surface reflectance, ρ_s, as function of wavelength, λ, by simultaneous measurement of upwelling radiance, L_u and downwelling planar irradiance, E_d at bottom of atmosphere:

$$\rho_s(\lambda) = \pi \frac{L_u(\lambda)}{E_d(\lambda)} \tag{4}$$

The abovewater measurement method for water-leaving radiance reflectance is more complex than for the surface reflectance given in (4) because of an extra term relating to the skyglint correction [49] using a measurement of the downwelling sky radiance, L_d. The latter term may exacerbate the problem of wiggles in the case where different radiometers with different wavelength scale are used to measure L_u and L_d, e.g. in the 3-sensor systems popular for shipborne measurements [36,50,51]. However, the cause of wiggles is most clearly explained and illustrated for the simpler ρ_s measurand.

In the following description of simulation conditions, we use many simplifying assumptions so that the results show most clearly the processes generating spectral wiggles. In more realistic conditions (smoothly varying but not constant surface reflectance, smoothly varying but not constant downwelling irradiance, etc.) the spectral wiggles will be quite similar, but superimposed on a smoothly varying but not constant surface reflectance. For cases where downwelling irradiance is

affected by multiple atmospheric absorption features over a short wavelength range, the wiggle-generation process is essentially the same, although more complex to present.

2.2 Model assumptions - simulated surface, atmosphere and radiometers

We suppose that the true surface reflectance is a constant value, $\rho_s(\lambda) = \rho_{s0}$, over an arbitrary short wavelength range, e.g. 15 nm.

We suppose that the true extraterrestrial downwelling irradiance, F_0, is also constant over this wavelength range and that the downward atmospheric transmittance, $t_d(\lambda)$, is equal to one except for an atmospheric absorption feature centered on wavelength λ_0 with rectangular SRF with full width λ_{w0} and transmittance, $t_d = t_{d0}$, giving the true downwelling irradiance:

$$E_t(\lambda) = F_0 * \begin{cases} 1 & \lambda < \lambda_0 - \lambda_{w0}/2 \\ t_{d0} & \lambda_0 - \lambda_{w0}/2 \le \lambda \le \lambda_0 + \lambda_{w0}/2 \\ 1 & \lambda > \lambda_0 + \lambda_{w0}/2 \end{cases} \tag{5}$$

The true upwelling radiance is then given trivially by:

$$L_t(\lambda) = L_{u0} * \begin{cases} 1 & \lambda < \lambda_0 - \lambda_{w0}/2 \\ t_{d0} & \lambda_0 - \lambda_{w0}/2 \le \lambda \le \lambda_0 + \lambda_{w0}/2 \\ 1 & \lambda > \lambda_0 + \lambda_{w0}/2 \end{cases} \tag{6}$$

where $L_{u0} = \rho_{s0} F_0/\pi$.

Now suppose that measurements are made with a hyperspectral radiometer system where the irradiance and radiance sensor have spectral sampling interval of ΔE and ΔL with a square wave SRF for each detector with spectral width of λ_{wE} and λ_{wL} respectively. The n detectors will be labelled $1 \ldots i_E \ldots n$, where i_E is the detector with largest central wavelength less than λ_0 for the irradiance measurement with corresponding j_L for the radiance measurement. The central wavelength of the irradiance and radiance sensor are shifted with respect to the absorption feature central wavelength λ_0 by offsets λ'_E and λ'_L respectively, giving central wavelength for detector i:

$$\lambda^i_{cE} = \lambda_0 + \lambda'_E + (i - i_E) * \Delta E \tag{7}$$

$$\lambda^j_{cL} = \lambda_0 + \lambda'_L + (j - j_L) * \Delta \mathrm{L} \tag{8}$$

Thus the irradiance SRF are given by:

$$\omega^i_E(\lambda) = \begin{cases} 0 & \lambda < \lambda^i_{cE} - \lambda_{wE}/2 \\ 1 & \lambda^i_{cE} - \lambda_{wE}/2 \le \lambda \le \lambda^i_{cE} + \lambda_{wE}/2 \\ 0 & \lambda > \lambda^i_{cE} + \lambda_{wE}/2 \end{cases} \tag{9}$$

and a similar expression for the radiance SRF, $\omega^i_L(\lambda)$.

This notation is illustrated in Figure 6.

The irradiance measured by each detector is then given by

$$E_i = \frac{\int \omega^i_E(\lambda) E_t(\lambda) d\lambda}{\int \omega^i_E(\lambda) d\lambda} \tag{10}$$

And, as shown later, the true square wave forms for $E_t(\lambda)$ and $L_t(\lambda)$ become trapezoidal wave forms with smoothing and widening of $E_t(\lambda)$ in the measurements in the case where the absorption band is narrower than the SRF of a detector, i.e. for $\lambda_{w0} \le \lambda_{wE}$.

An example of how the finite SRF of the detector affects the measured E_i in the vicinity of an under-resolved atmospheric absorption band, is illustrated in

Figure 7. The depth of the absorption feature of real depth t_{d0} is smoothed in the measured spectrum to the shallower depth $t_{d0}\frac{\lambda_{w0}}{\lambda_{wE}}$. The shape of the measured spectrum is, however, not necessarily symmetric about λ_0, but may be asymmetric according to the offset, λ'_E, of the sampling wavelengths with respect to the centre of the absorption band λ_0 – see Figure 8. This dependence of the measured signal on central wavelength and sampling interval has been demonstrated previously[52] for the O_2-A band near 762 nm.

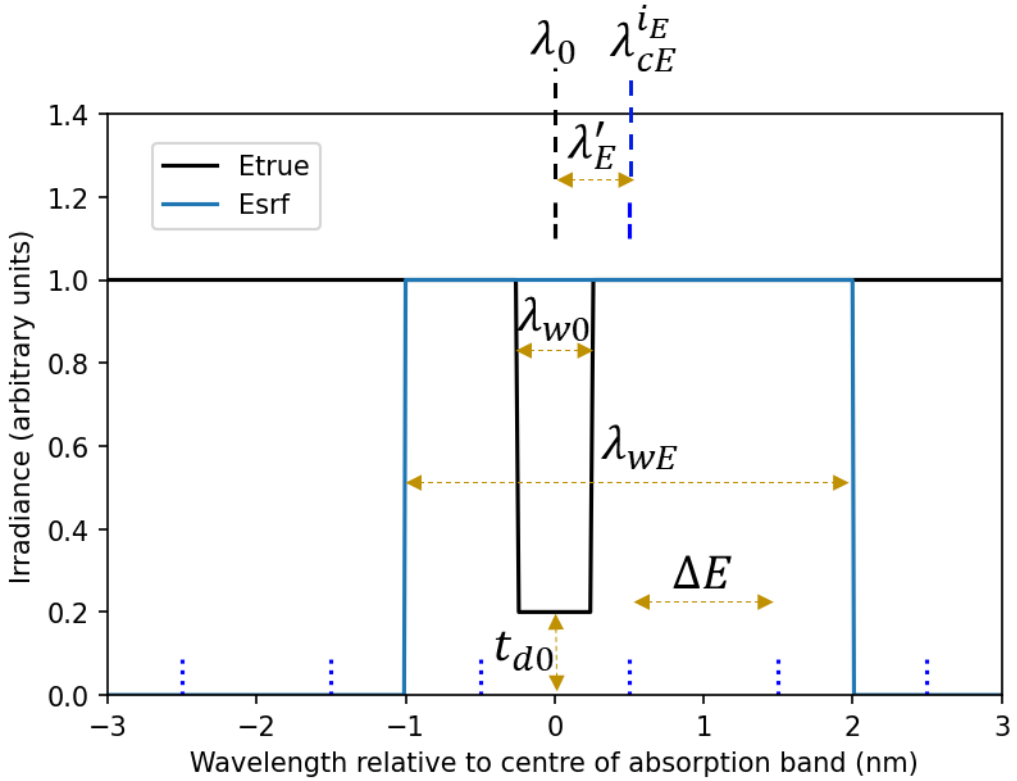

Figure 6. Schematic showing definitions of terminology for the true irradiance spectrum, $E_t(\lambda)$, labelled as "Etrue" (black solid line), the SRF, $\omega_E^i(\lambda)$, for the one detector labelled as "Esrf" (blue solid line) with central wavelength $\lambda_{cE}^{i_E}$, the central wavelengths of all detectors, λ_{cE}^{i} (short vertical dotted lines), and the downward transmittance, t_{d0}.

The case is simulated here of the HYPSTAR® radiometer, which has a single spectrometer but different optical paths for radiance and irradiance giving an offset between the wavelength scales for irradiance and radiance measurements, simulated here as different λ_{cE}^i and λ_{cL}^j.

In the HYPSTAR® radiometer processing, the reflectance output is made at the central wavelengths of the radiance measurements, with irradiance interpolated from the two bounding λ_{cE}^i to the single radiance wavelength λ_{cL}^j, where $\lambda_{cE}^i \leq \lambda_{cL}^j < \lambda_{cE}^{i+1}$ by

$$E_{LINT}^j\left(\lambda_{cL}^j\right) = \left(1 - w_{LIN}^j\right) * E_i + w_{LIN}^j * E_{i+1} \tag{11}$$

Where the linear interpolation weighting is used:

$$w_{LIN}^j = \left(\frac{\lambda_{cL}^j - \lambda_{cE}^i}{\Delta E}\right) \tag{12}$$

And the reflectance on the radiance wavelength scale is given by

$$\rho_s(\lambda_{cL}^j) = \pi \frac{L_j}{E_{LINT}^j} = \pi \frac{L_j}{\left\{E_i\left(\frac{\lambda_{cE}^{i+1} - \lambda_{cL}^j}{\Delta E}\right) + E_{i+1}\left(\frac{\lambda_{cL}^j - \lambda_{cE}^i}{\Delta E}\right)\right\}} \tag{13}$$

The linear interpolation method is designed to give perfect results in the case where the true spectral variation of the measurand is linear and gives results accurate to $O(\Delta E)^2$ for more complex variability according to Taylor analysis.

2.3 Model-adjusted interpolation of irradiance

For the case of significant unresolved spectral variability, we propose here a new irradiance model-based interpolation method weighted according to the expected sub-SRF spectral variability of $E_t(\lambda)$.

Thus, the linear interpolation is now performed between model-adjusted measurements E_i and E_{i+1}, replacing (11) by

$$E_{MINT}(\lambda_{cL}^j) = (1 - w_{LIN}^j) * \left(\frac{E_{mod}(\lambda_{cL}^j)}{E_{mod}(\lambda_{cE}^i)}\right) * E_i + w_{LIN}^j * \left(\frac{E_{mod}(\lambda_{cL}^j)}{E_{mod}(\lambda_{cE}^{i+1})}\right) * E_{i+1} \tag{14}$$

Where $E_{mod}(\lambda_{cL}^j)$ is obtained by convolution of a modelled higher resolution irradiance spectrum, $E_{mod}(\lambda)$, over the instrument SRF, i.e.

$$E_{mod}(\lambda_{cE}^i) = \frac{\int \omega_E^i(\lambda) E_{mod}(\lambda) d\lambda}{\int \omega_E^i(\lambda) d\lambda} \tag{15}$$

This form has the useful properties that:

- (14) reduces to the conventional linear interpolation over wavelength for the case where E_{mod} is constant over the short wavelength range
- (14) gives simply $E_{MINT}(\lambda_{cL}^j) = \alpha E_{mod}(\lambda_{cL}^j)$ in the case where the measurements E_i and E_{i+1} follow perfectly the shape of $E_{mod}(\lambda)$ with $E_i / E_{mod}(\lambda_{cE}^i) = E_{i+1} / E_{mod}(\lambda_{cE}^{i+1}) = \alpha$, and
- (14) gives $E_{MINT}(\lambda_{cL}^j) = E_{mod}(\lambda_{cL}^j)$ in the case where the measurements E_i and E_{i+1} take perfectly the values of $E_{mod}(\lambda)$ at λ_{cE}^i and λ_{cE}^{i+1}.

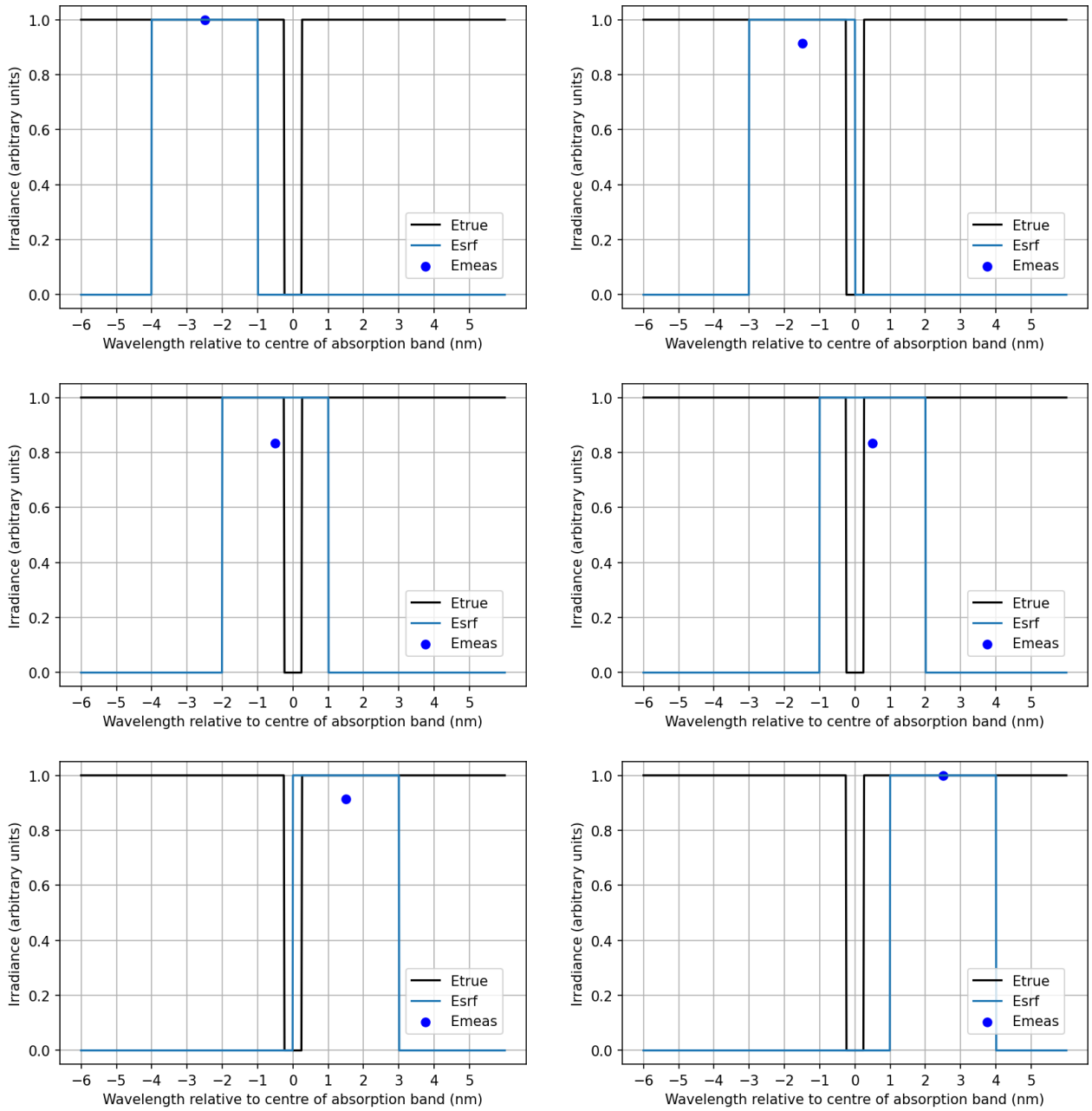

Figure 7. Six examples of overlap for successive detectors, $i = i_E - 3 \ldots i_E + 2$, between an atmospheric absorption band with true downwelling irradiance, E_t, (solid black line, "Etrue") and the SRF of a radiometer detector (solid blue line) shown as function of relative wavelength, $\lambda - \lambda_0$. The measured irradiance E_i (blue dots, "Emeas") obtained by convolution of irradiance with SRF are shown at central wavelength, λ_{cE}^{i}. In this simulation the atmospheric absorption feature has $t_{d0} = 0$, with width $\lambda_{w0} = 0.5\ nm$. The irradiance sensor has spectral resolution $\lambda_{wE} = 3\ nm$, spectral sampling every $\Delta E = 1\ nm$, with central wavelengths offset with respect to λ_0 by $\lambda_E' = 0.5\ nm$.

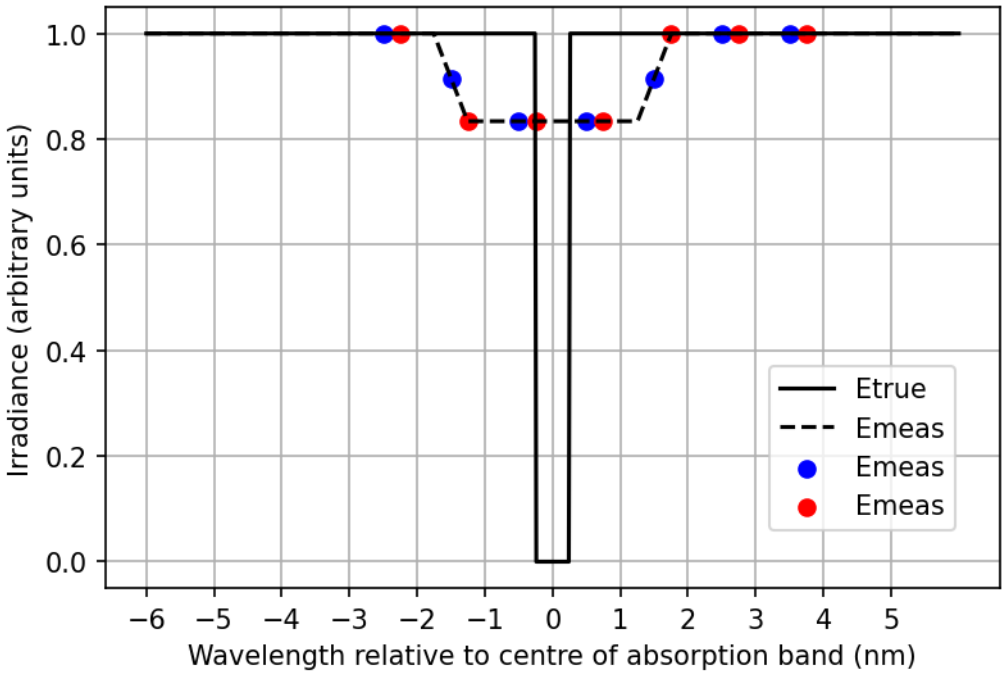

Figure 8. Combination of measurements from all detectors of the simulated hyperspectral irradiance sensor showing the true downwelling irradiance, E_t, (solid black line, "Etrue"), the measurements at all detectors for the example of Figure 7 with $\lambda'_E = 0.5\ nm$ (blue dots), the measurements at all detectors for a similar irradiance sensor with $\lambda'_E = 0.75\ nm$ (red dots), and the envelope of measurements (dashed line) from all possible offsets, λ'_E. Other simulation conditions as in Figure 7.

3. RESULTS

3.1 Simulation results with conventional linear interpolation of irradiance

While λ'_E and λ'_L may take any value in the range $[0,\Delta E)$ we present simulations here for 4 values of $\lambda'_E = 0, 0.25, 0.5, 0.75\ nm$ and 4 values of $\lambda'_L = 0, 0.25, 0.5, 0.75\ nm$ to demonstrate typical results for ρ_s.

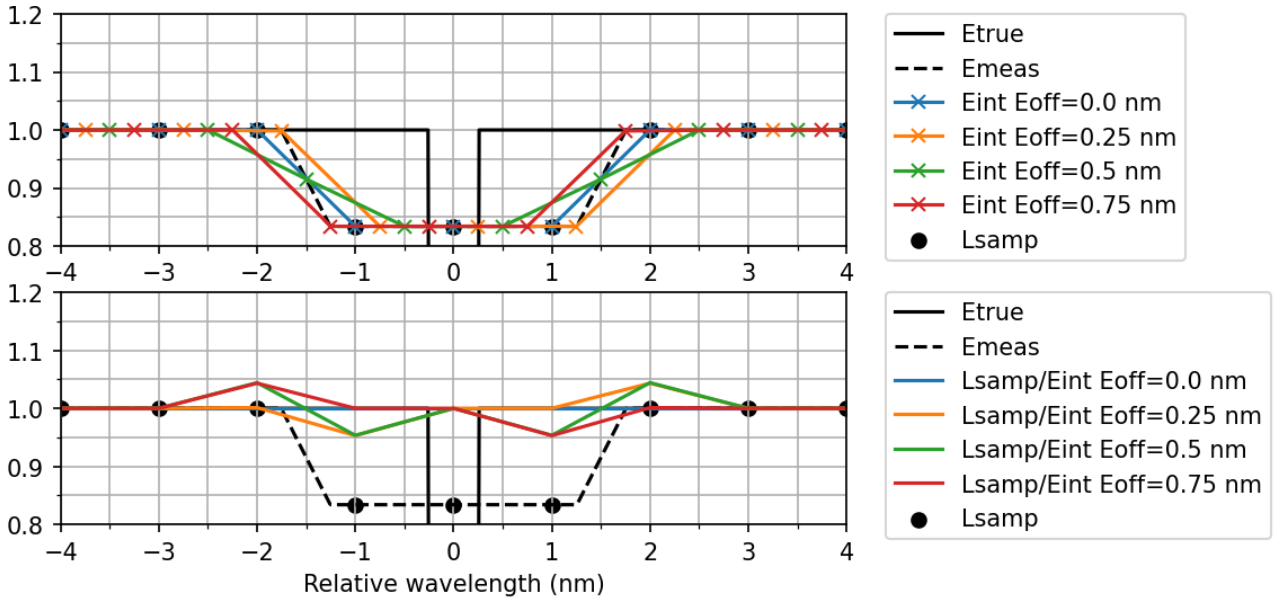

Figure 9. Simulations for $\lambda_L^{'} = 0\ nm$ with $t_{d0} = 0$, $\lambda_{w0} = 0.5\ nm$, $\lambda_{wE} = \lambda_{wL} = 3\ nm$, $\Delta E = \Delta L = 1\ nm$ and 4 values of $\lambda_E^{'} = 0, 0.25, 0.5, 0.75\ nm$ ("Eoff"). [top] Results show true irradiance (solid black line, "Etrue"), E_t, envelope of all possible values of E_i (dashed black line, "Emeas") corresponding to all possible values of $\lambda_E^{'}$, specific examples of E_i corresponding to the 4 values of $\lambda_E^{'}$ (4 coloured markers), continuous E spectra obtained by linear interpolation using (11) between E_i for the 4 values of $\lambda_E^{'}$ (4 coloured lines joining markers) and sampled values of radiance (black dots), L_i, for this $\lambda_L^{'} = 0\ nm$. [bottom] Corresponding values of $\rho_s(\lambda_{cL}^j)/\pi = L(\lambda_{cL}^j)/E(\lambda_{cL}^j)$ obtained from sampled L_j and sampled then interpolated $E_{LINT}(\lambda_{cL}^j)$.

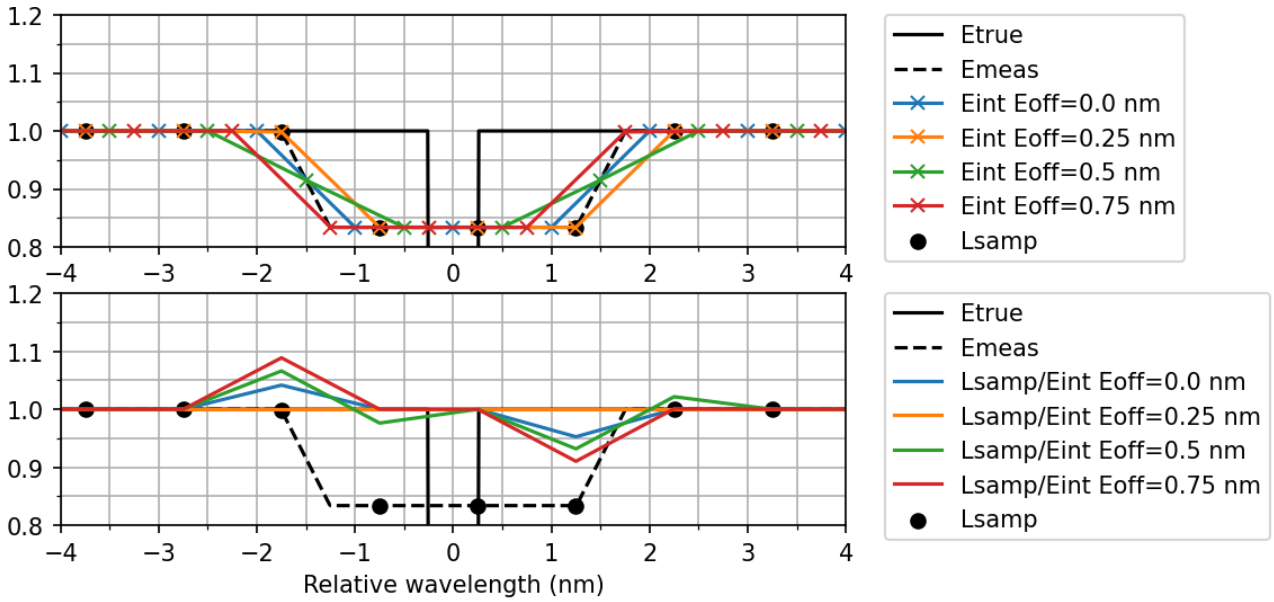

Figure 10. Simulation conditions and result labelling as for Figure 9 except that $\lambda_L^{'} = 0.25\ nm$.

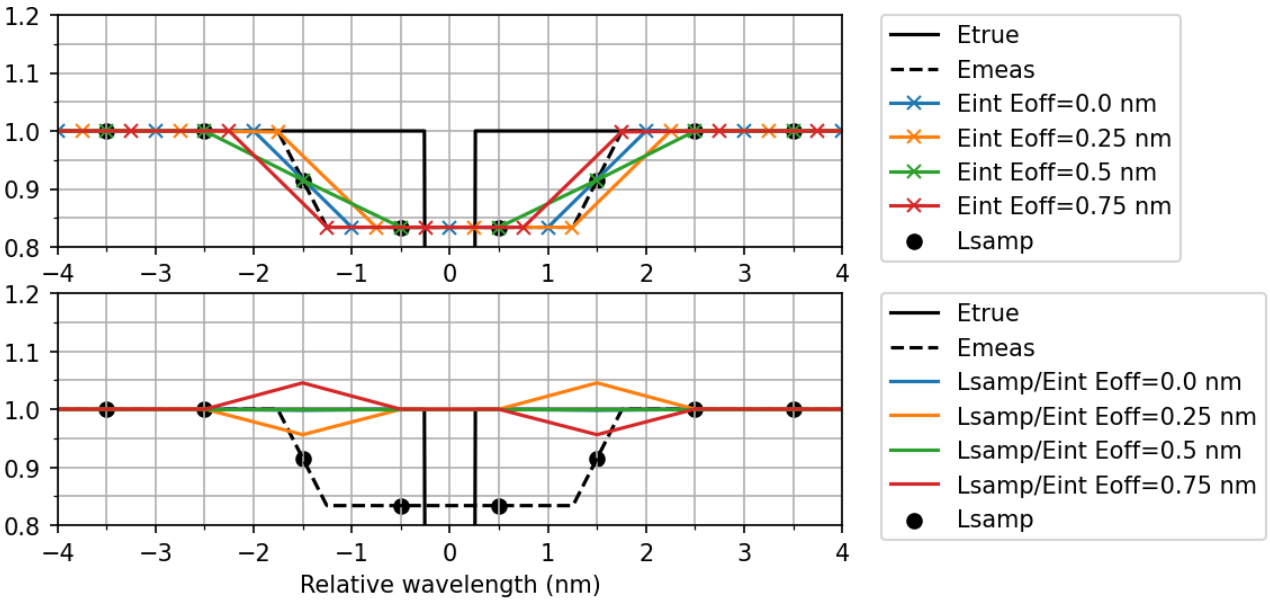

Figure 11. Simulation conditions and result labelling as for Figure 9 except that $\lambda_L^{'} = 0.5\ nm$.

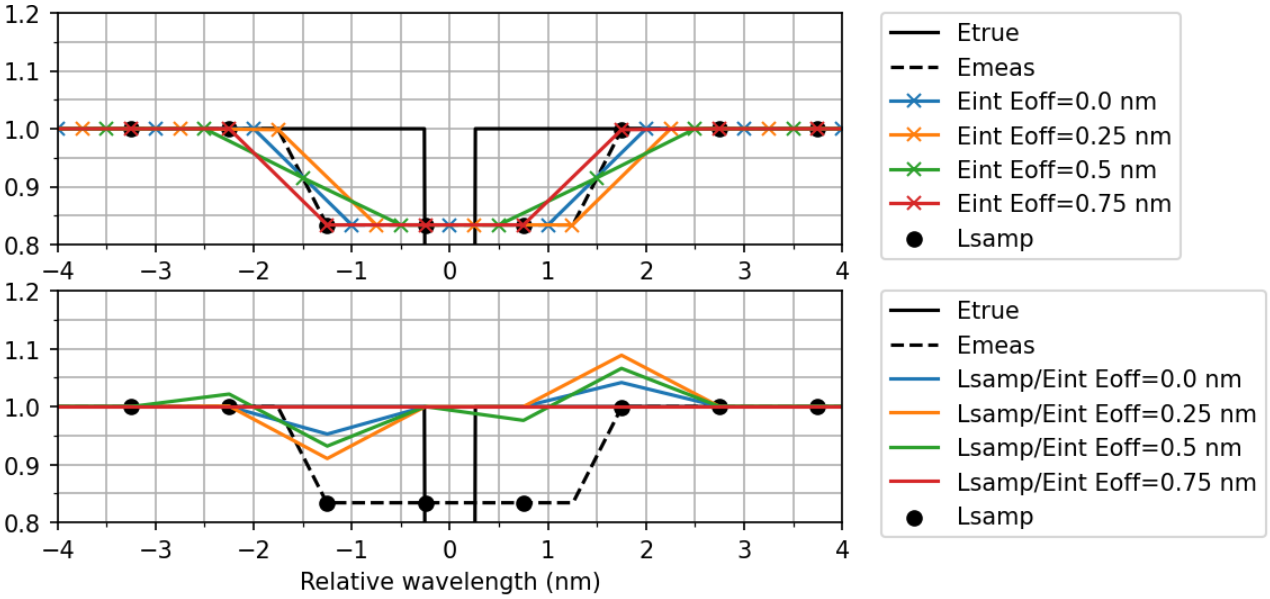

Figure 12. Simulation conditions and result labelling as for Figure 9 except that $\lambda_L^{'} = 0.75\ nm$.

From the results of Figure 9-Figure 12, it is clear that the ρ_s is measured perfectly in the cases where $\lambda'_L = \lambda'_E$, and the special case $\lambda'_L = 0.5\ nm$ and $\lambda'_E = 0.0\ nm$ (Figure 11 green line) but shows wiggles in all other cases with $\lambda'_L \neq \lambda'_E$. This can be seen either as one positive and one negative wiggle either side of the absorption feature or more complex wiggle shapes, e.g. case $\lambda'_L = 0.75\ nm$ and $\lambda'_E = 0.5\ nm$ (Figure 12 green line). All such wiggles will generate an artificial 2nd derivative of ρ_s.

3.2 Simulation results with new model-adjusted interpolation of irradiance

If the newly-proposed model-adjusted interpolation of irradiance (14) is used with $E_{mod}(\lambda)$ obtained from the envelope E_i ("Emeas") spectrum shown in the results of Figure 9-Figure 12, i.e. $E_{mod}(\lambda^i_{cE}) = E_i$ in all cases, then it is trivial for these simulations that

$$E_{MINT}(\lambda^j_{cL}) = E_{mod}(\lambda^j_{cL}) \tag{16}$$

and

$$\rho_s(\lambda^j_{cL}) = \pi L(\lambda^j_{cL})/E(\lambda^j_{cL}) = 1$$

i.e. the constant surface reflectance spectrum is perfectly conserved, without wiggles.

What is not yet known is how this model-adjusted interpolation will perform in practice with real measurements and how any uncertainties in the modelled spectrum E_{mod} or the radiometer characteristics $\lambda_{wE}, \lambda_{wL}, \Delta E, \Delta L$ will propagate through the model-adjusted interpolation.

It seems obvious that $E_{mod}(\lambda)$ should be defined at least as a function of sun zenith angle. If information is available on other atmospheric parameters (absorbing gas concentrations, aerosols, atmospheric pressure) at the time of the measurement then $E_{mod}(\lambda)$ could be further improved. Uncertainties in the modelled spectrum $E_{mod}(\lambda)$ may also arise from assumptions of the atmospheric radiative transfer model, including extraterrestrial solar irradiance, spectral absorption cross-section of each gas, model spectral resolution, etc.

4. CONCLUSIONS AND FUTURE PERSPECTIVES

While the new generation in situ hyperspectral radiometers and spaceborne spectrometers will provide hyperspectral water reflectance data that could be used for discriminating between phytoplankton species, the explicit or implicit use of second wavelength derivatives may lead to severe contamination of data in the presence of unresolved atmospheric absorption bands. In addition to the well-known problems of random noise and interband calibration, it is shown here for a simulated in situ hyperspectral radiometer system that a wavelength offset between measured radiance and irradiance can generate short wavelength scale variability, termed "wiggles". These wiggles could be removed by appropriately weighted (not linear, but irradiance model-adjusted) spectral interpolation of irradiance that takes account of the expected unresolved variability of true irradiance over the instrument SRF. In practice the true irradiance is unknown, but it is suggested here that a reasonable estimation of the unresolved spectral variability of true irradiance (e.g. from atmospheric radiative transfer modelling with inputs for sun zenith angle, aerosol type and concentration, absorbing gas concentrations and atmospheric pressure) could give significant reduction of spurious wiggles.

The present study has clearly illustrated one process causing spectral wiggles and provides a clear way forward for solving the problem of spurious wiggles generated by wavelength scale difference between irradiance and radiance. Next, the proposed irradiance-weighted spectral interpolation method should be tested on real measured irradiance spectra before implementation in the HYPERNETS operational processing chains [53,54]. The impact of uncertainties, in the proposed atmospheric radiative transfer modelling and associated inputs and in the knowledge of instrument characteristics (central wavelengths, shape and width of SRF, etc.), on the effectiveness of the proposed irradiance-weighted spectral interpolation method for wiggle-removal/reduction needs to be studied.

The present study has demonstrated the wiggle-generation process for an in situ radiometer system with different wavelength scales for radiance and irradiance. For spaceborne reflectance measurements the irradiance needed for reflectance normalization does not come from a separate measurement but is obtained from tabulated data for extraterrestrial solar irradiance and modelling of diffuse atmospheric transmittance from TOA to BOA using estimation of

aerosols potentially derived from the spaceborne radiance measurement. It is speculated here that imperfections in the modelling of irradiance (via atmospheric transmittance) and/or in the SRF used for convolution of the modelled irradiance for spaceborne reflectance data would generate similar wiggles to those found here for in situ radiometry, since the wavelength scale used for irradiance would be different from that used (implicitly) in the radiance measurement.

Further study is needed to:

- Test the current proposal for irradiance model weighted interpolation in the case of real in situ measurements
- Initiate similar studies on the wiggle generation processes for spaceborne data

The latter will ensure that the full potential of spaceborne hyperspectral reflectance data can be realised, avoiding the need for and the information loss entailed in the current crude spectral-averaging techniques used for wiggle suppression.

The current study focusses on the second derivative of reflectance and is directly relevant for algorithms that explicitly use the second derivative of reflectance. However, the process described is presumably relevant also for neural network and other algorithms used for phytoplankton group discrimination unless the spectral wiggle artefacts found in satellite data are removed or correctly modelled in the training dataset.

ACKNOWLEDGEMENTS

This study was funded by the European Union's Horizon 2020 research and innovation programme under grant agreement No 775983 ("HYPERNETS"). The colleagues of the HYPERNETS project are acknowledged for useful discussions.

REFERENCES

[1] Alonso, K., Bachmann, M., Burch, K., Carmona, E., Cerra, D., De los Reyes, R., Dietrich, D., Heiden, U., Hölderlin, A., Ickes, J., and others., "Data products, quality and validation of the DLR earth sensing imaging spectrometer (DESIS)," Sensors **19**(20), 4471 (2019).

[2] Loizzo, R., Guarini, R., Longo, F., Scopa, T., Formaro, R., Facchinetti, C. and Varacalli, G., "PRISMA: The Italian hyperspectral mission," IGARSS 2018-2018 IEEE Int. Geosci. Remote Sens. Symp., 175–178, IEEE (2018).

[3] Kaufmann, H., Segl, K., Chabrillat, S., Hofer, S., Stuffler, T., Mueller, A., Richter, R., Schreier, G., Haydn, R. and Bach, H., "EnMAP a hyperspectral sensor for environmental mapping and analysis," 2006 IEEE Int. Symp. Geosci. Remote Sens., 1617–1619, IEEE (2006).

[4] Gorman, E. T., Kubalak, D. A., Patel, D., Mott, D. B., Meister, G., Werdell, P. J., and others., "The NASA Plankton, Aerosol, Cloud, ocean Ecosystem (PACE) mission: an emerging era of global, hyperspectral Earth system remote sensing," Sens. Syst. -Gener. Satell. XXIII **11151**, 78–84, SPIE (2019).

[5] Blackburn, G. A., "Hyperspectral remote sensing of plant pigments," J. Exp. Bot. **58**(4), 855–867 (2007).

[6] Goyens, C., Lavigne, H., Dille, A. and Vervaeren, H., "Using Hyperspectral Remote Sensing to Monitor Water Quality in Drinking Water Reservoirs," 21, Remote Sens. **14**(21), 5607 (2022).

[7] Ruddick, K. G., et al., "WATERHYPERNET: Automated in situ measurements of hyperspectral water reflectance for satellite validation ... and more.," presented at Oceans from Space, 2022, Venice.

[8] Lehmann, M. K., Gurlin, D., Pahlevan, N., Alikas, K., Conroy, T., Anstee, J., Balasubramanian, S. V., Barbosa, C. C., Binding, C., Bracher, A., and others., "GLORIA-A globally representative hyperspectral in situ dataset for optical sensing of water quality," Sci. Data **10**(1), 100 (2023).

[9] Vermote, E., Tanré, D., Deuzé, J. L., Herman, M., Morcette, J. J. and Kotchenova, S. Y., "Second simulation of the satellite signal in the solar spectrum-vector (6SV)," 6S User Guide Version 3, 134 (2006).

[10] Coddington, O. M., Richard, E. C., Harber, D., Pilewskie, P., Woods, T. N., Snow, M., Chance, K., Liu, X. and Sun, K., "Version 2 of the TSIS-1 Hybrid Solar Reference Spectrum and Extension to the Full Spectrum," Earth Space Sci. **10**(3), e2022EA002637 (2023).

[11] Nechad, B., Ruddick, K. G. and Neukermans, G., "Calibration and validation of a generic multisensor algorithm for mapping of turbidity in coastal waters," presented at SPIE European International Symposium on Remote Sensing, 2009.

[12] Gitelson, A., "The peak near 700 nm on radiance spectra of algae and water: Relationships of its magnitude and position with chlorophyll concentration," Int J Remote Sens **13**(17), 3367–3373 (1992).
[13] Gilerson, A. A., Gitelson, A. A., Zhou, J., Gurlin, D., Moses, W., Ioannou, I. and Ahmed, S. A., "Algorithms for remote estimation of chlorophyll-a in coastal and inland waters using red and near infrared bands," Opt. Express **18**(23), 24109–24125 (2010).
[14] Lavigne, H., Ruddick, K. and Vanhellemont, Q., "Monitoring of high biomass Phaeocystis globosa blooms in the Southern North Sea by in situ and future spaceborne hyperspectral radiometry," Remote Sens. Environ. **282**, 113270 (2022).
[15] Stumpf, R. P. and Werdell, P. J., "Adjustment of ocean color sensor calibration through multi-band statistics," Opt. Express **18**(2), 401–412 (2010).
[16] Mizuochi, H., Tsuchida, S., Obata, K., Yamamoto, H. and Yamamoto, S., "Combination of Cross-and Inter-Band Radiometric Calibrations for a Hyperspectral Sensor Using Model-Based Spectral Band Adjustment," Remote Sens. **12**(12), 2011 (2020).
[17] Lavigne, H. and Ruddick, K., "Inter-band calibration for hyperspectral water remote sensing: demonstration for CHRIS-PROBA," 2021 IEEE Int. Geosci. Remote Sens. Symp. IGARSS, 7771–7774, IEEE (2021).
[18] Babin, M. and Stramski, D., "Light absorption by aquatic particles in the near-infrared spectral region," Limnol. Oceanogr. **47**(3), 911–915 (2002).
[19] Lee, Z.-P., Carder, K. L. and Arnone, R., "Deriving inherent optical properties from water color: a multi-band quasi-analytical algorithm for optically deep waters," Appl. Opt. **41**, 5755–5772 (2002).
[20] Doxaran, D., Cherukuru, N. and Lavender, S. J., "Apparent and inherent optical properties of turbid estuarine waters: measurements, empirical quantification relationships and modeling," Appl. Opt. **45**(10), 2310–2324 (2006).
[21] Babin, M., Stramski, D., Ferrari, G. M., Claustre, H., Bricaud, A., Obolensky, G. and Hoepffner, N., "Variations in the light absorption coefficients of phytoplankton, nonalgal particles and dissolved organic matter in coastal waters around Europe," J. Geophys. Res. **108**(C7), 3211, doi:10.1029/2001JC000882 (2003).
[22] Kou, L., Labrie, D. and Chylek, P., "Refractive indices of water and ice in the 0.65μm to 2.5μm spectral range," Appl. Opt. **32**, 3531–3540 (1993).
[23] Loisel, H., Nicolas, J.-M., Sciandra, A., Stramski, D. and Poteau, A., "Spectral dependency of optical backscattering by marine particles from satellite remote sensing of the global ocean," J. Geophys. Res. **111**(C09024) (2006).
[24] Morel, A., "Light scattering by seawater. Experimental results and theoretical approach. (Diffusion de la lumière par les eaux de mer. Résultats expérimentaux et approche théorique)." (1973).
[25] Röttgers, R., McKee, D. and Utschig, C., "Temperature and salinity correction coefficients for light absorption by water in the visible to infrared spectral region," Opt. Express **22**(21), 25093–25108 (2014).
[26] Bidigare, R., Morrow, J. and Kiefer, D., "Derivative analysis of spectral absorption by photosynthetic pigments in the western Sargasso Sea," J. Mar. Res. **47**(2), 323–341 (1989).
[27] Astoreca, R., Rousseau, V., Ruddick, K., Knechciak, C., Van Mol, B., Parent, J.-Y. and Lancelot, C., "Development and application of an algorithm for detecting Phaeocystis globosa blooms in the Case 2 Southern North Sea waters," J. PLANKTON Res. **31**(3), 287–300 (2009).
[28] Organelli, E., Bricaud, A., Antoine, D. and Uitz, J., "Multivariate approach for the retrieval of phytoplankton size structure from measured light absorption spectra in the Mediterranean Sea (BOUSSOLE site)," Appl. Opt. **52**(11), 2257–2273 (2013).
[29] Aguirre-Gomez, R., Weeks, A. and Boxall, S., "The identification of phytoplankton pigments from absorption spectra," Int. J. Remote Sens. **22**(2–3), 315–338 (2001).
[30] Lubac, B., Loisel, H., Guiselin, N., Astoreca, R., Artigas, L. F. and Mériaux, X., "Hyperspectral and multispectral ocean color inversions to detect Phaeocystis globosa blooms in coastal waters.," J. Geophys. Res. **113**(C06026) (2008).
[31] Torrecilla, E., Stramski, D., Reynolds, R. A., Millán-Núñez, E. and Piera, J., "Cluster analysis of hyperspectral optical data for discriminating phytoplankton pigment assemblages in the open ocean," Remote Sens. Environ. **115**(10), 2578–2593 (2011).
[32] Uitz, J., Stramski, D., Reynolds, R. A. and Dubranna, J., "Assessing phytoplankton community composition from hyperspectral measurements of phytoplankton absorption coefficient and remote-sensing reflectance in open-ocean environments," Remote Sens. Environ. **171**, 58–74 (2015).

[33] Hedley, J. D., Mobley, C. D. and Sundman, L. K., "HYDROLIGHT 5.3 Technical Documentation," Tiverton (2017).
[34] Pope, R. M. and Fry, E. S., "Absorption spectrum (380-700nm) of pure water. II. Integrating cavity measurements," Appl. Opt. **36**, 8710–8723 (1997).
[35] Smith, R. C. and Baker, K. S., "Optical properties of the clearest nautral waters (200-800nm)," Appl. Opt. **20**, 177–184 (1981).
[36] Ruddick, K., De Cauwer, V., Park, Y. and Moore, G., "Seaborne measurements of near infrared water-leaving reflectance: The similarity spectrum for turbid waters," Limnol. Oceanogr. **51**(2), 1167–1179 (2006).
[37] Gresho, P. M. and Lee, R. L., "Don't suppress the wiggles—They're telling you something!," Comput. Fluids **9**(2), 223–253 (1981).
[38] Mueller, J. L., Davis, C., Arnone, R., Frouin, R., Carder, K., Lee, Z. P., Steward, R. G., Hooker, S., Mobley, C. D. and McLean, S., "Above-water radiance and remote sensing reflectance measurements and analysis protocols (Chapter 3)," [Ocean Optics protocols for satellite ocean color sensor validation Revision 4, Volume III], NASA, Greenbelt, MD, USA, 21–31 (2003).
[39] Castagna, A., Johnson, B. C., Voss, K., Dierssen, H. M., Patrick, H., germer, T., Sabbe, K. and Vyverman, W., "Uncertainty in global downwelling plane irradiance estimates from sintered polytetrafluoroethylene plaque radiance measurements," Appl. Opt. **58**(16), 4497–4511 (2019).
[40] Ruddick, K., Voss, K., Banks, A. C., Boss, E., Castagna, A., Frouin, R. J., Hieronymi, M., Jamet, C., Johnson, B. C., Kuusk, J., Lee, Z., Ondrusek, M., Vabson, V. and Vendt, R., "A review of protocols for Fiducial Reference Measurements of downwelling irradiance for validation of satellite remote sensing data over water," Remote Sens. **11**(15), 1742 (2019).
[41] Lavigne, H. and Ruddick, K., "The potential use of geostationary MTG/FCI to retrieve chlorophyll-a concentration at high temporal resolution for the open oceans," Int. J. Remote Sens. **39**(8), 2399–2420 (2018).
[42] Bourg, L. and Delwart, S., "MERIS instrument calibration," Second MERIS AATSR Calibration Geophys. Valid. Workshop Frascati Italy, 20–24 (2006).
[43] Eplee, R. E., Meister, G., Patt, F. S., Barnes, R. A., Bailey, S. W., Franz, B. A. and McClain, C. R., "On-orbit calibration of SeaWiFS," Appl. Opt. **51**(36), 8702–8730 (2012).
[44] Zibordi, G., Mélin, F., Voss, K. J., Johnson, B. C., Franz, B. A., Kwiatkowska, E., Huot, J.-P., Wang, M. and Antoine, D., "System vicarious calibration for ocean color climate change applications: Requirements for in situ data," Remote Sens. Environ. **159**, 361–369 (2015).
[45] Salim, S. G. R., Fox, N. P., Theocharous, E., Sun, T. and Grattan, K. T. V., "Temperature and nonlinearity corrections for a photodiode array spectrometer used in the field," Appl. Opt. **50**(6), 866–875 (2011).
[46] Pacheco-Labrador, J., Ferrero, A. and Martín, M. P., "Characterizing integration time and gray-level-related nonlinearities in a NMOS sensor," Appl. Opt. **53**(32), 7778–7786 (2014).
[47] "The TSIS-1 Hybrid Solar Reference Spectrum - Coddington - 2021 - Geophysical Research Letters - Wiley Online Library.", <https://agupubs.onlinelibrary.wiley.com/doi/10.1029/2020GL091709> (10 August 2023).
[48] Steven, D., Preusker, R., Bourg, L., Santer, R., Ramon, D. and Fischer, J., "MERIS in-flight spectral calibration" (2006).
[49] Mobley, C. D., "Estimation of the remote-sensing reflectance from above-surface measurements," Appl. Opt. **38**, 7442–7455 (1999).
[50] Brando, V., Lovell, J., King, E., Boadle, D., Scott, R. and Schroeder, T., "The Potential of Autonomous Ship-Borne Hyperspectral Radiometers for the Validation of Ocean Color Radiometry Data," Remote Sens. **8**(2), 150 (2016).
[51] Alikas, K., Vabson, V., Ansko, I., Tilstone, G. H., Dall'Olmo, G., Nencioli, F., Vendt, R., Donlon, C. and Casal, T., "Comparison of Above-Water Seabird and TriOS Radiometers along an Atlantic Meridional Transect," 10, Remote Sens. **12**(10), 1669 (2020).
[52] Damm, A., Erler, A., Hillen, W., Meroni, M., Schaepman, M. E., Verhoef, W. and Rascher, U., "Modeling the impact of spectral sensor configurations on the FLD retrieval accuracy of sun-induced chlorophyll fluorescence," Remote Sens. Environ. **115**(8), 1882–1892 (2011).
[53] Goyens, C., De Vis, P. and Hunt, S. E., "Automated Generation of Hyperspectral Fiducial Reference Measurements of Water and Land Surface Reflectance for the Hypernets Networks," 2021 IEEE Int. Geosci. Remote Sens. Symp. IGARSS, 7920–7923 (2021).
[54] De Vis, P., Goyens, C., Hunt, S. and Vanhellemont, Q., "Generating Hyperspectral Reference Measurements for Surface Reflectance from the Land and Water HYPERNETS Networks," Front. Remote Sens. Prep.